

Oxidation and Strain in Free-standing Silicon Nanocrystals


Bruno P. Falcão,^{1,*} Joaquim P. Leitão,¹ Maria R. Soares,² Lídia Ricardo,³ Hugo Águas,³ Rodrigo Martins,³ and Rui N. Pereira^{1,4}

¹*Departamento de Física and I3N, Universidade de Aveiro, Campus Universitário de Santiago, 3810-193 Aveiro, Portugal*

²*Laboratório Central de Análises, Universidade de Aveiro, Campus Universitário de Santiago, 3810-193 Aveiro, Portugal*

³*CENIMAT/I3N, Departamento de Ciência dos Materiais, Faculdade de Ciências e Tecnologia, Universidade Nova de Lisboa, CEMOP-UNINOVA, 2829-516 Caparica, Portugal*

⁴*Walter Schottky Institut and Physik-Department, Technische Universität München, Am Coulombwall 4, 85748 Garching, Germany*

 (Received 22 November 2018; revised manuscript received 21 January 2019; published 21 February 2019)

The investigation of surface-induced lattice-strain effects in free-standing silicon nanocrystals (Si NCs) is fundamental in view of the materialization of nanosilicon-based technologies that exploit the unique properties of silicon at the nanoscale. In this work, a comprehensive investigation in free-standing Si NCs is performed, aimed at unveiling physical phenomena related to surface oxidation upon exposure to air, from which strongly surface-dependent lattice strain is found. Raman and infrared spectroscopy techniques are used to monitor the time evolution of the oxidation, through which a clear correlation between the formation of a superficial native oxide and the appearance of compressive strain in the nanocrystals' core is found, which increases continuously as the oxidation progresses. By comparing experimental data with simulations using an improved phonon confinement model, it is concluded that strain is negligible in H-terminated nanocrystals with sizes of approximately 3 nm. After long-term natural oxidation, the compressive stress imposed by the native oxide shell is estimated to be 1.2 GPa. The results presented here link the time-dependent oxidation phenomenon with the experimental observation of compressive strain in free-standing Si NCs, clarifying contradicting results found in the literature, and demonstrate a simple route for the deconvolution of confinement and strain effects in low-dimensional structures using Raman spectroscopy.

DOI: [10.1103/PhysRevApplied.11.024054](https://doi.org/10.1103/PhysRevApplied.11.024054)

I. INTRODUCTION

Over the last decades, low-dimensional semiconductor structures based on silicon have been the focus of intensive scientific research owing to their unique properties and potential technological applications. In this regard, silicon nanocrystals (Si NCs) combine desirable optoelectronic features [1–3], including high luminescence quantum yields, with a variety of advantageous processing approaches [3,4], ranging from colloidal methods to plasma synthesis, which resulted in practical demonstrations of light-emitting devices [5–7], sensors [8–10], optical communications [11], field-effect transistors [12–15], solar cells [16–20], energy storage solutions [21,22], and medical and biological applications [23–25], amongst many others. Due to the huge surface-to-volume ratio, the properties of Si NCs are highly sensitive to surface

effects and the surrounding environment. As an example, the efficiency of electronic impurity doping may change by several orders of magnitude depending on the medium around the Si NCs [26]. In fact, the sensitivity of the nanocrystals' behavior to surface effects can be exploited to controllably adapt these materials for specific applications. For instance, in optoelectronic applications, surface engineering can offer an additional degree of freedom to the quantum-confinement effect in tailoring the emission wavelength and enhancing the luminescence quantum yield [27–32]. Surface engineering also provides a means to improve the size control and to explore collective effects observed in closed-packed Si NCs (e.g., ultra-efficient carrier multiplication) [29,33]. However, lattice strain is inherently associated with any form of surface modification of nanocrystals and this may affect the properties of nanocrystals in various ways, such as alteration of electronic structure, transformation of phase, or buckling [34]. Therefore, the understanding of surface-induced

*bfalcao@ua.pt

lattice-strain effects in Si NCs is very important for the materialization of nanotechnologies that exploit the unique properties of silicon at the nanoscale.

Perhaps the most relevant method of surface engineering of Si NCs is the growth of a silicon oxide shell on the surface of free-standing Si NCs (hereafter mentioned as silicon nanoparticles, Si NPs). Crystalline Si NPs are typically synthesized with a hydrogen termination [3,4,35] and the formation of a native silicon oxide shell upon exposure to ambient atmosphere is the so far most frequently applied technique to produce Si—SiO₂ core-shell nanoparticles. The presence of an oxide shell on the Si NPs confers water solubility and biocompatibility [36] and also strongly affects their optical emission [37,38]. For instance, in a recent work, Botas *et al.* observed a strong increase of the luminescence quantum yield in surface-oxidized silicon nanoparticles (Si NPs) in comparison to Si NPs with a hydrogen termination, due to the inhibition of internanoparticle charge transfer [39]. Importantly, it has been suggested by several groups that the presence of an oxide shell generates interfacial stress, which has the potential of influencing both the structural and the optical properties of the nanocrystals [40–44]. The structural deformation, i.e., strain, that the oxide shell exerts over the crystalline core of the Si NPs is far from being understood. Although it is generally considered that strain increases with the thickening of the oxide shell, the literature available for Si NPs reports contradicting results about whether the strain is strictly compressive, tensile, or a mixture of both depending on the particle size and on the extent of the surface oxidation [40–47]. In the case of Si NCs embedded in an oxide matrix, several studies show that the nanocrystals are under compression mostly due to the lattice mismatch and different compressibilities between the surrounding matrix and the nanocrystals [42,48–54]. Similar conclusions have been drawn in other systems, such as in matrix-embedded Ge [55,56], CdSe [57], and CdS_{1-x}Se_x [58] nanocrystals, and CdSe/CdS core-shell nanocrystals [59].

In this work, we carry out a research effort in view of linking the evolution of the oxidation phenomenon in crystalline Si NPs with the appearance and the nature of lattice strain. A thorough spectroscopic characterization using infrared absorption is performed to evaluate the surface oxidation of the Si NPs. Additionally, we also monitor the evolution of the Raman spectra along the oxidation process and compare the theoretically obtained variations of the Raman shift (Ω) and linewidth (Γ) with those measured experimentally. Our results indicate that in H-terminated Si NPs the lattice strain is negligible and that the continuous growth of an oxide shell leads to the appearance of an increasing compressive strain in the Si NP core throughout the whole oxidation process. The impact of this compressive strain on relevant properties of Si NPs are discussed. Moreover, we discuss the implications of our results for

the applicability of the Raman technique in the study of nanosilicon materials, which has been widely applied by researchers over the last 30 years.

II. EXPERIMENTAL DETAILS

Free-standing Si NCs in the powder form and with a surface termination with Si—H bonds (H-termination) are synthesized from gas phase in a silane (SiH₄) nonthermal plasma reactor under a discharge pressure of 3 Torr, radiofrequency (rf) power 75 W, electrode distance 16 mm, Ar flow 35 sccm, SiH₄ flow 0.65 sccm, and deposition time approximately 30 min. Two depositions are made following this recipe. In one deposition (dep. no. 1), the Si NP powder is directly collected on a mesh placed at the bottom of the reactor, whereas in the other deposition (dep. no. 2) a borosilicate glass substrate (ProSciTech Pty Ltd), previously coated with Au, is placed over the mesh to collect the Si NP powder both on this substrate and on the mesh. In both cases, the deposits are immediately sealed under N₂ atmosphere after deposition, then transferred to a N₂-purged glovebox with extremely low concentration of oxygen and moisture (< 1 ppm).

Several samples are prepared based on the Si NP powders synthesized in both depositions. For x-ray diffraction (XRD) measurements the Si NP powders (dep. no. 1) are analyzed in the as-grown form. For Raman spectroscopy experiments, a solution containing Si NPs (dep. no. 1) dispersed in 1,2-dichlorobenzene (99%, Sigma-Aldrich) is spin coated onto Al-metalized borosilicate glass substrate (ProSciTech Pty Ltd). For TEM experiments, a highly diluted solution of this Si NPs dispersion is pipetted onto ultrathin carbon film grids supported by a lacey carbon film with a 400 copper mesh (PELCO). For the electron-paramagnetic-resonance- (EPR) spectroscopy studies, a solution based on Si NP powders from dep. no. 2 is prepared in a similar fashion, pipetted to a quartz tube, and sealed after full evaporation of the solvent. The infrared spectra are collected on the Si NPs deposited directly on the Au-covered glass substrate in dep. no. 2. This sample is also investigated by Raman spectroscopy. All samples are prepared in the glovebox.

Raman scattering measurements are performed at room temperature (290 K) in backscattering configuration using a Jobin-Yvon LabRam HR 800 spectrometer equipped with a Peltier-cooled (203 K) CCD detector and with a 50× long focal distance objective (0.5 numerical aperture). The samples are inserted in a Linkam THMS600 stage and kept under vacuum conditions (< 10⁻² mbar) during all measurements. The 532 nm line of a diode-pumped solid-state (DPSS) laser (Laser Quantum) is used as excitation source, at a power density below 10³ W/cm². A piece of an intrinsic Si wafer is used to calibrate the Raman spectrometer and the measured spectra are corrected assuming the value of 521 cm⁻¹ as the room-temperature Stokes

shift of the optical phonon mode in bulk crystalline Si (*c*-Si). XRD measurements are performed in a PANalytical X'Pert MPD diffractometer in the Bragg-Brentano geometry using Cu K_α radiation. The mean crystallite diameter is evaluated by means of the Scherrer equation and also by carrying out a Rietveld refinement analysis. High-resolution TEM measurements are carried out in an energy-filtered 200 kV JEOL 2200FS system equipped with an energy dispersive spectroscopy (EDS) detector. EPR spectroscopy is performed in absorption mode at room temperature with a continuous-wave spectrometer (Bruker) mounted with a X-band microwave bridge and a lock-in amplifier with a magnetic field modulation of 100 kHz, resulting at low microwave powers in unsaturated absorption-derivative signals as comprehensively checked with microwave power series measurements. The infrared measurements are performed on a Bruker Vertex 80v FTIR spectrometer equipped with a Hyperion microscope unit. Data are collected at room temperature and ambient conditions in the backscattering reflectance mode using a liquid N₂-cooled MCT detector (D316, Bruker) and a 15× objective. A piece of Au-coated glass is used to collect the background spectrum.

III. RESULTS AND DISCUSSION

A. Characterization of as-grown Si NPs

Following the general route of low-pressure plasma synthesis of Si NPs [4,60–63], the low-temperature decomposition of silane in our rf plasma reactor yields densely packed ensembles of spherical crystalline Si NPs. The deposits are analyzed before long-term exposure to air (hereby denoted as as-grown Si NPs) by HRTEM in order to investigate their structural properties. As shown in Fig. 1(a), the crystalline Si NPs are characterized by a rather narrow lognormal size distribution with mean diameter $\bar{D} = 2.9 \pm 0.1$ nm and standard deviation $\sigma = 0.15 \pm 0.02$ nm. This narrow size distribution is in line with the results reported for Si NPs synthesized by gas-phase methods determined by TEM [45,61,64–66], Raman spectroscopy [64,65], and particle mass spectrometry [60]. Crowe *et al.* [67] also obtained size distributions for Si NPs produced through the annealing of Si supersaturated oxide films very close to that obtained for our Si NPs. We note that size distributions determined from Raman spectroscopy may not be reliable [68]. In order to confirm the average size of as-grown Si NPs we measure XRD diffraction pattern in the Bragg-Brentano geometry [see Fig. 1(b)]. We estimate the mean crystallite size by the Scherrer equation applied for the (111) peak (assuming a shape factor for spherical particles $K = 0.89$ [69]) and also by a Rietveld refinement analysis, obtaining values of 2.8 ± 0.1 and 3.1 ± 0.2 nm, respectively. Both values are in line with that found with TEM, thereby

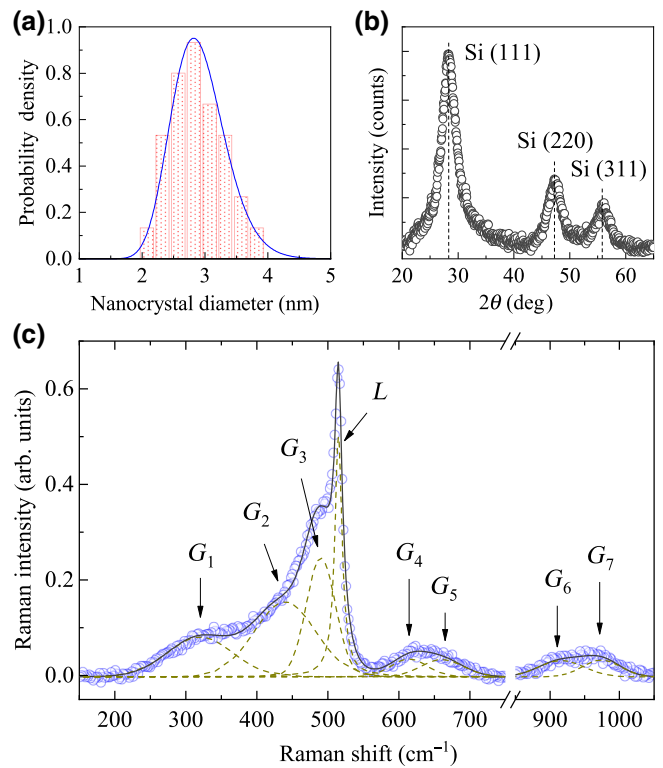


FIG. 1. (a) Size distribution, (b) XRD diffraction pattern (after baseline removal), and (c) Raman spectrum from as-grown Si NPs. The solid line in (c) illustrates the fit to the experimental spectrum assuming several Gaussian (G_i) and one Lorentzian (L) components (dashed lines).

strengthening the TEM analysis and thus the confidence on the determined size distribution.

Raman spectroscopy measurements are performed with a low excitation power density to prevent *in-situ* light-induced structural modifications of the nanocrystals, such as (photo-)oxidation, due to the presence of residual moisture and oxygen [70–72], and local heating effects, which could result in a misinterpretation of the Raman spectrum [40,73]. The Raman spectrum of as-grown Si NPs shown in Fig. 1(c) evidences several features due to first-order Raman scattering, up to approximately 550 cm^{-1} , and weaker structures spread over the $550\text{--}1050 \text{ cm}^{-1}$ spectral range, due to second-order Raman scattering (arising from quantum-confinement effects [74]). In order to identify its origin, the spectrum is deconvoluted with several Gaussian components (G_i) and one Lorentzian curve (L) [see dashed lines in Fig. 1(c)], whose fitting parameters are listed in Table I.

The main feature observed in the spectrum of Fig. 1(c) (peak L) is ascribed to lattice vibrations related with (degenerated) longitudinal and transversal optical phonons [LTO (Γ)] near the center of the Brillouin zone (Γ point), arising from the crystalline core of the Si NPs [75]. Due to confinement effects, the peak is centered at 515 cm^{-1}

TABLE I. Raman peaks observed in the Raman spectrum of as-grown Si NPs [Fig. 1(c)]. All values are given in cm^{-1} .

Peak	Ω	Γ	Assignment	Refs.
G_1	320 ± 5	108 ± 3	Surfacelike optical	[46,75–78]
G_2	440 ± 4	102 ± 5	phonon modes	
G_3	490 ± 1	49 ± 2		
L	515 ± 1	12 ± 1	LTO (Γ)	
G_4	614 ± 19	61 ± 18	Si—H, 2 LA,	[74,79–85]
G_5	661 ± 29	70 ± 27	TO+TA	
G_6	916 ± 10	77 ± 12	2 TO	[74,80,84–86]
G_7	974 ± 7	64 ± 8		

and has a full-width-at-half-maximum (Γ , also termed here as “linewidth”) of approximately 12 cm^{-1} , being significantly redshifted and broadened with respect to that observed in bulk *c*-Si under similar conditions (peaking at 521 cm^{-1} and with a natural linewidth of 3 cm^{-1}). Measurements repeated on other spots of the sample, i.e., different ensembles of nanocrystals, revealed that the peak position variation of L around 515 cm^{-1} is lower than the experimental error ($\pm 1 \text{ cm}^{-1}$). This provides a further evidence that the average nanocrystal size is homogenous and also shows that there are no significant local heating effects. Otherwise, differences in the thermal conductivity owing to nanocrystal ensembles with different morphologies would lead to variations in the peak position and linewidth amongst the different spectra [73].

Conversely, expressive variations of the order of several cm^{-1} are found on the peak position of components G_1 – G_3 when measuring on different spots of the sample. Following recent works [30,46,68,75–78], the analysis of the Raman spectrum should take into account zone center phonon modes as well as surfacelike modes, where the competing influences of under-coordination, bond length and angle variations, and quantum-confinement effects lowers the vibrational frequencies of optical phonons with respect to that observed in bulk *c*-Si. In order to consider these effects, one can picture a small Si NP as a core-shell-like structure, where the core is a typical crystal with fourfold coordinated Si atoms (as in bulk) and the shell is a somewhat disordered spherical surface comprising the outermost atomic layers of the nanoparticle, where some of the atoms are two and threefold coordinated (the number of onefold coordinated atoms is very small) [46,77,78]. In this scenario, the phonon DOS from the core of the nanoparticle displays bulklike phonon modes mostly correlated to *c*-Si zone center modes, namely peak L , whose frequency shift is influenced by quantum-confinement effects [75,78]. On the other hand, the surface DOS exhibits specific modes, mainly related with vibrations from undercoordinated Si atoms with contracted and distended bond lengths and deformed bond angles with respect to the crystalline phase [46,75,76,78]. The number of (surface) vibrational

modes contributing to the Raman spectrum increases as the nanocrystal diameter decreases because the increase in surface-to-volume ratio results in a larger proportion of distorted surface Si—Si bonds. This leads to an increase of the relative contribution of components G_1 – G_3 to the Raman spectrum in small nanocrystals [75,76,78]. Hence, variations on the morphology of the nanocrystal surface could explain why the position of the G_1 – G_3 peaks varies significantly. Indeed, since these variations do not affect the nanocrystal size, the position of peak L does not shift significantly (influenced mainly by confinement effects), as observed in the experiments. The observation of Si—H_{*x*} ($x = 1, 2, 3$) vibrations in the second-order Raman spectrum and in the infrared spectra (discussed below) further supports the role of a disordered surface and the correspondent assignment of components G_1 – G_3 to disorder-activated optical phonon modes.

The spectral feature at 550 – 750 cm^{-1} , described by components G_4 and G_5 , coincides with the position of the Si—H bond bending or wagging band that is commonly observed in hydrogenated amorphous silicon (*a*-Si:H), [79–83] as well as with second-order Raman peaks related with the longitudinal acoustical mode overtone (2LA) and combination of transverse optical and acoustic modes (TO + TA) of different critical points (X , Σ) [74,79,80,83–85]. We note that surface hydride bands are observed in infrared spectroscopy studies, as shown below. The broad band between 850 – 1050 cm^{-1} is also fitted with two Gaussian components (G_6 , G_7) and can be explained considering overtones of few transverse optical phonons (2 TO) from several critical points (L , X , W) [74, 80,84–86]. We must stress that an unambiguous assignment of the G_4 – G_7 bands is hindered by the variations in the peak positions due to quantum-confinement effects [74] and by the low signal-to-noise ratio, which result in significant errors in the peak position and linewidth values obtained from the fits (as shown in Table I). Despite this uncertainty, it is interesting to investigate the intensity ratio of second- to first-order Raman scattering [$\eta = I(2\text{TO})/I(\text{LTO})$], since additional information concerning the properties of the nanocrystals can be retrieved. Thus, from our fitting, we estimate that the relative integrated intensity of the 2 TO band [$I(G_6)+I(G_7)$] with respect to the integrated intensity of the LTO peak [$I(L)$] is of the order of 0.5. This value far exceeds those typically found for *a*-Si ($\eta < 0.25$) [79,85], bulk *c*-Si ($\eta = 0.1$) [79], and silicon nanowires ($\eta = 0.11$) [87], but are of the same order of those found in free-standing [88] and oxide-embedded [89] Si NCs of similar dimensions. The observation of high ratios η can be attributed to an increase of the scattering cross section near the electronic resonance transitions, which reflects a stronger electron-phonon coupling in these nanoparticulate systems [88–90]. Moreover, high values of the η ratio have also been related with the decrease of crystal size and to the presence of surface

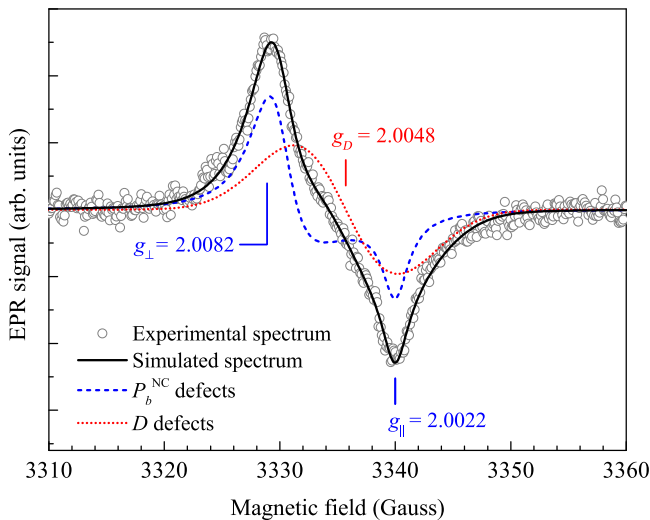


FIG. 2. EPR spectrum from as-grown Si NPs (open circles), together with computer simulation (solid curve), taking into account a powder pattern of axial symmetry (dashed curve) and an isotropic resonance (dotted curve).

disorder [74], which is consistent with our observation of the disorder-related Raman bands described above as well as with the disordered dangling bond defects addressed in the following.

EPR measurements are performed in view of gathering additional information about the Si NPs surface. Figure 2 depicts the experimental (open circles) EPR spectrum of as-grown Si NPs. Following our approach in previous works [91,92], the spectrum is simulated (solid curve) considering two different types of silicon dangling bonds: an axially symmetric powder pattern (dashed curves) with $g_{\perp} = 2.0082$ and $g_{\parallel} = 2.0022$ typical of defects at the interface between crystalline silicon and an oxide (P_b^{NC} defects), and one isotropic component (dotted curves) with $g_D = 2.0048$ characteristic of dangling bonds in a disordered environment (D defects). The former component reveals the presence of some surface oxygen in the form of Si—O—Si bonds already in the as-grown Si NPs, which is confirmed by the FTIR data presented below. The observation of D defects in the Si NPs supports the presence of a disordered amorphouslike Si phase at the surface of the Si NPs, as revealed by the Raman data presented above.

B. Ambient-oxidation of Si NPs

Figure 3 shows selected regions of FTIR spectra recorded for as-grown Si NPs (air exposure time $t_{ox} = 0.5$ h) and after long-term exposure to air ($t_{ox} = 3433$ h). The spectrum recorded for $t_{ox} = 0.5$ h (solid line) displays a structured band with three components in the range $2000\text{--}2170\text{ cm}^{-1}$ that is attributed to Si—H stretching vibrations of $\text{Si}_{4-x}\text{—Si—H}_x$ ($x = 1, 2, 3$) surface hydride groups [91–96]. Two additional peaks with lower intensity

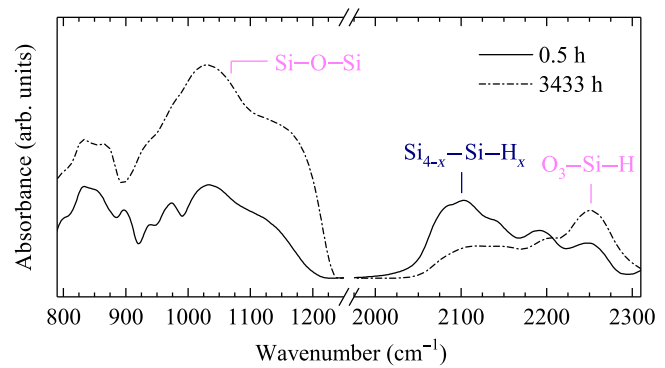


FIG. 3. FTIR spectra in the range of stretching modes of Si—O—Si and Si—H bonds recorded for as-grown Si NPs (solid line) and after long-term exposure to air (dot-dashed line).

are also observed in the high-energy side of the spectrum (at approximately 2190 and approximately 2250 cm^{-1}), due to the stretching of oxidized hydride groups ($\text{O}_2\text{—Si}_2\text{—H}$ and $\text{O}_2\text{—Si—H}_2$, and $\text{O}_3\text{—Si—H}$, respectively) on the surface of the nanocrystals, [95–98] most likely originating from small oxygen contamination of the as-grown Si NPs during synthesis, similar to previous studies of Si NPs synthesized with the same method [91,92]. The presence of a small amount of surface oxygen is also revealed by the structured broad band observed in the range $925\text{--}1250\text{ cm}^{-1}$, mainly due to stretching of Si—O—Si surface bonds [91,92]. The low-energy side of the spectrum ($800\text{--}925\text{ cm}^{-1}$) evidences a structured feature that can be assigned to several vibrations, namely the bending modes of Si—O—Si and $\text{O}_3\text{—Si—H}$, degenerate and symmetric deformation modes of Si—Si—H₃, and scissoring and wagging modes of Si—Si—H₂ [93,94].

The spectrum shows several changes after long-term exposure to air (see dot-dashed line in Fig. 3). There are strong increases in the intensity of the bands in the regions $925\text{--}1250$ and $2225\text{--}2300\text{ cm}^{-1}$, mainly due to Si—O—Si and $\text{O}_3\text{—Si—H}$ bonds, respectively. Conversely, a significant decrease in intensity of the $\text{Si}_{4-x}\text{—Si—H}_x$ hydrides band is observed.

The evolution of the intensity of the bands of Si—O—Si bonds and surface hydrides $\text{Si}_{4-x}\text{—Si—H}_x$ as a function of t_{ox} is evaluated by numerical integration in the $925\text{--}1250$ and $2000\text{--}2170\text{ cm}^{-1}$ spectral ranges, respectively. The obtained dependencies are depicted in the semi-log plot of Fig. 4. As can be seen, the surface of the Si NPs exhibits nearly no oxidation during an initial period of time, commonly referred to as the *induction period* [91,92]. After approximately 100 h, the oxidation proceeds logarithmically, in line with the experimental data reported by Pereira *et al.* for ambient-air-oxidized Si NPs synthesized through a similar nonthermal rf plasma approach [91,92]. The intensity dependence of the Si—O—Si band with t_{ox} is fitted with the Elovich equation (see dashed line in Fig. 4),

which describes the dynamics of physical processes and reactions on solid surfaces [91,92,99],

$$n_m(t_{\text{ox}}) = \lambda_m t_m \ln \left(1 + \frac{t_{\text{ox}}}{t_m} \right), \quad (1)$$

where $n_m(t_{\text{ox}})$ is the amount of reaction products, λ_m is the reaction rate, and t_m is the characteristic time. From the fitting, we estimate a characteristic time $t_m = 98$ h, which is indicated by the dot-dashed vertical line in Fig. 4. It is interesting to note that the induction period estimated for our Si NPs is very close to the one (88 h) found by Pereira *et al.* for Si NPs produced under similar conditions [91,92]. In addition, in the interval of air-exposure times investigated in our experiments, the oxidation process does not seem to reach saturation. Such a saturation is expected to take place only after a few thousand hours of air exposure [91,92].

The evolution of the Raman spectra with t_{ox} is also monitored under controlled measurement conditions. In these studies, the sample is probed over time (i) repeatedly on the same spots (denoted hereafter as “fixed-spot experiment”) and (ii) on random spots (“random-spot experiment”). The inset in Fig. 5 depicts a few spectra from a fixed-spot experiment (i), where a strong increase in the background intensity is observed as the oxidation evolves. In order to investigate this behavior, we estimate the value of the Raman intensity (arbitrarily) at 1100 cm^{-1} and plot the results for both types of experiments (i) and (ii) as a function of t_{ox} . As shown in Fig. 5, the evolution of the background intensity of the Raman spectra with t_{ox} resembles the behavior of our FTIR data for both datasets (see circle symbols in Fig. 4), i.e., the intensity increases strongly

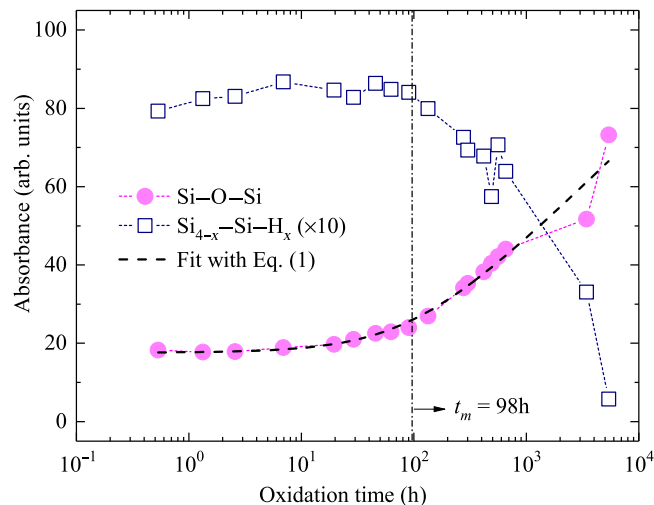


FIG. 4. Dependence of the intensity of FTIR bands from the surface species Si—O—Si and $\text{Si}_{4-x}\text{—Si—H}_x$ as a function of the oxidation time. The dashed line represent the fitting curve to the Si—O—Si data using Eq. (1).

only after a certain time of air exposure. Interestingly, there is a small increase in intensity, approximately one order of magnitude earlier, for the fixed-spot data (approximately 10 h) in comparison to that observed for the random-spot data (approximately 100 h). Notwithstanding, the main time threshold of the two datasets corresponds to the induction period of $t_m = 98$ h estimated by the Elovich equation for the FTIR data (see vertical dashed line in Fig. 5). This remarkable quantitative agreement between data from two independent experimental techniques strongly suggests that the physical mechanisms responsible for the increase of the Raman spectrum background are directly linked to the oxidation of the nanocrystals. High-intensity backgrounds in Raman spectra have been observed recently for large free-standing Si NPs under intensive excitation power, which was attributed to blackbody radiation [100]. Since our Si NPs are much smaller and are probed under low-excitation conditions such an explanation is unlikely to apply in our case. We propose that the high-intensity Raman background is related to the tail of a photoluminescence band originating from the oxidation of the Si NPs. Recently, Botas *et al.* observed a substantial increase in the light-emission quantum yield of surface-oxidized Si NPs when compared to the same Si NPs with a H-passivated surface, due to the inhibition of internanocrystal charge transfer (imposed by the oxide shell) [39]. A significant increase of the PL intensity and a blueshift of the emission during the oxidation of Si NPs have also been reported by several groups [37,38,101,102]. Moreover, we note that a small intensity increase occurs earlier for the fixed-spot experiment because the continuous

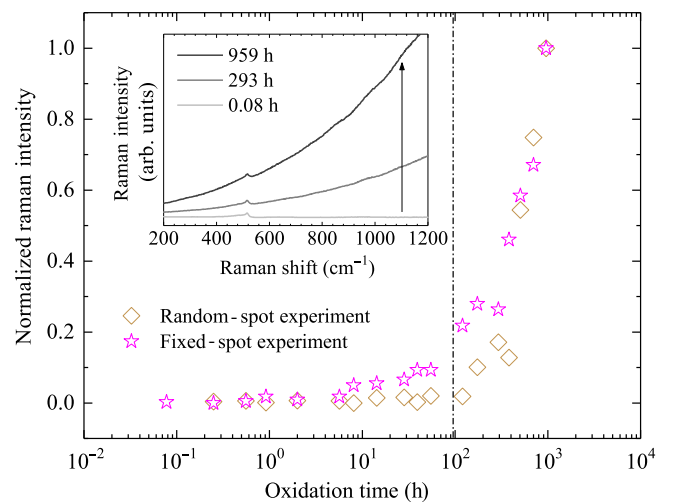


FIG. 5. Raman intensity at 1100 cm^{-1} as a function of oxidation time, extracted from Raman spectra measured on random spots and on fixed spots. The intensity is normalized to the value corresponding to the measured highest oxidation time (approximately 1000 h). The inset shows Raman spectra from the fixed-spot dataset for different t_{ox} values.

laser illumination promotes a small photo-oxidation of the nanocrystals within these measurement spots. This is a clear evidence that measuring Raman spectra repeatedly in the same spot, even under highly controlled conditions, induces structural changes in the nanocrystals, namely, the growth of a small superficial oxide.

The spectra measured as a function of oxidation time are fitted following the model described above [see Fig. 1(c)], after careful removal of the luminescence-related background using a high-order polynomial function. The obtained relation between position (Ω) and linewidth (Γ) of the LTO peak (component L), associated to scattering from the crystalline core of the Si NPs, is plotted in Fig. 6 for both random-spot and fixed-spot experiments as diamond and star symbols, respectively. We note that the data from the fixed-spot dataset are average values for each t_{ox} determined from three experiments (i), i.e., from measurements performed on three different spots. As can be seen, as the oxidation evolves the peak shifts moderately towards lower frequencies and broadens significantly, which in a first approximation can be explained by a confinement effect due to a decrease of the nanocrystal size at the expense of the oxide growth at its surface. Although the data are somewhat scattered, we do not identify meaningful differences between the two datasets. This observation suggests that in terms of vibrational properties the oxidation occurs in the same fashion in the two cases, i.e., regardless of being solely promoted by exposure to air or, in addition, being also affected by the weak laser illumination. Globally, the relation Ω vs Γ follows a linear trend characterized by a variation $d\Omega/d\Gamma = -0.19$, as illustrated by the red solid line $\Omega(\Gamma)_{\text{exp}}$ in Fig. 6.

In order to investigate the expected relation between Ω and Γ , we carry out theoretical simulations within the framework of the phonon confinement model (PCM), following the formalism reported recently by our group [68]. Accordingly, the Raman spectra are simulated considering the effects of anisotropy and splitting of the optical phonon dispersions, which are fundamental to retrieve reliable information concerning the frequency shift and line broadening of the Raman spectrum of nanocrystals [68]. We started by calculating the Raman spectrum of the as-grown nanocrystals considering the size distribution given above [see Fig. 1(a)], characterized by a mean nanocrystal diameter $\bar{D} = 2.9$ nm. Then, we simulated the evolution of the spectrum assuming that the nanocrystal size distribution changes with the evolution of the oxidation due to the growth of an oxide shell of thickness d_{ox} . Here, we considered a value of $d_{\text{ox}} = 0.3$ nm based on the literature reported for similar Si NPs oxidized in air [91], where the nanocrystal size was measured using XRD data before air exposure and after air exposure for a few thousand hours, which resulted in a range for the mean size $\bar{D} = 2.9\text{--}2.3$ nm. Moreover, other studies using TEM data concluded

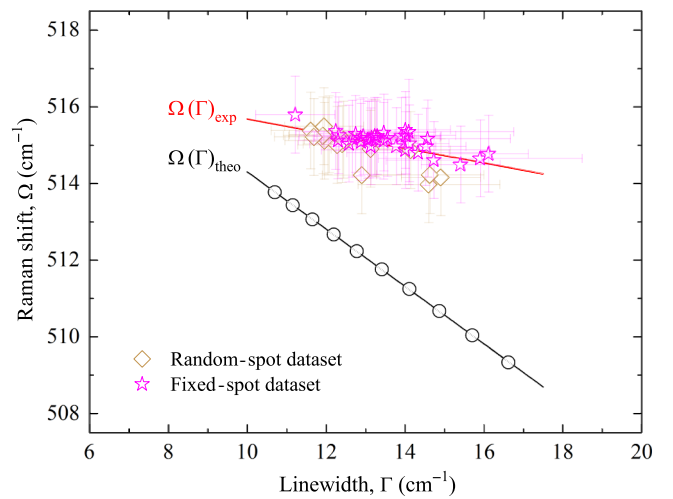


FIG. 6. Relation between the Raman peak’s position (Ω) and linewidth (Γ) measured on random spots and on fixed spots as a function of oxidation time. The circles represent the tendency obtained through the PCM [68], for \bar{D} values in the range 2.9–2.3 nm, i.e., for nanocrystal sizes ranging from the “as grown” to fully oxidized (admitting a 0.3-nm-thick oxide shell). Red and black solid lines represent linear fits to the experimental data [$\Omega(\Gamma)_{\text{exp}}$] and to the theoretical points [$\Omega(\Gamma)_{\text{theo}}$], respectively.

that the oxide thickness for air-exposed Si NPs with about 3 nm in diameter should be around 0.5 ± 0.2 nm [45]. In order to obtain the size distribution corresponding to each d_{ox} value, all size values comprising the size distribution, depicted in Fig. 1(a) for the case of $d_{\text{ox}} = 0$ nm ($\bar{D} = 2.9$ nm), are progressively subtracted by fractions of approximately 0.06 nm and the resulting size distribution is fitted with a lognormal function. We note that this is an important step in the simulation of accurate Raman spectra that considers the size distribution because, within this approach, the mean and standard deviation of the lognormal function varies as a function of surface oxidation (see Supplemental Material [103]).

After the simulation of each Raman spectrum for each d_{ox} , and \bar{D} and σ (see example in Ref. [68]), the corresponding values of Ω and Γ are estimated from the position of the peak maximum and absolute linewidth, respectively. The resulting relation Ω vs Γ , represented by open circles in Fig. 6, shows that the decrease of the mean nanocrystal size with increasing d_{ox} promotes a redshift and broadening of the Raman peak, qualitatively similar to the experimental observation. It is also interesting to note that the theoretical values of Γ are spread over approximately the same range of the experimental values (11–16 cm^{-1}). In spite of these similarities between theory and experiment, a few differences stand out: (i) there is a frequency shift of about 2 cm^{-1} separating $\Omega(\Gamma)_{\text{exp}}$ and $\Omega(\Gamma)_{\text{theo}}$ at the data corresponding to the as-grown nanocrystals; and (ii) the linear trend $\Omega(\Gamma)_{\text{theo}}$ is markedly steeper, with

$d\Omega/d\Gamma = -0.75$. These differences are discussed in more detail below in the scope of strain effects.

C. Strain in free-standing Si NPs

Prior to the oxidation, the 2 cm^{-1} separating the experimental data and the theoretical calculations can, in principle, be attributed to intrinsic errors associated with the experiments (approximately 1 cm^{-1}) and with the uncertainty of the phonon dispersion curves (approximately 1 cm^{-1}) used in the simulations [68]. At this oxidation stage, the lattice parameter a_{NC} of the nanocrystals, estimated through a Rietveld refinement of the XRD data ($a_{\text{NC}} = 5.429 \pm 0.002 \text{ \AA}$), is equal to that of the bulk ($a_{\text{bulk}} = 5.431 \text{ \AA}$) within the experimental error, suggesting that there is no lattice compression or dilation prior to the oxidation. Hence, we conclude that the amount of strain present prior to the oxidation should be negligible in our nanocrystals, as predicted theoretically for H-terminated silicon nanocrystals [46].

After long-term oxidation ($t_{\text{ox}} = 10^3 \text{ h}$), when the nanocrystals are smaller in size, the difference in frequency shift between $\Omega(\Gamma)_{\text{exp}}$ and $\Omega(\Gamma)_{\text{theo}}$ is $\sim 6 \pm 2 \text{ cm}^{-1}$. Such a difference can not be ascribed solely to intrinsic errors. Thus, we propose that the approximately $6 \pm 2 \text{ cm}^{-1}$ deviation is due to compressive strain in the nanocrystals. In this context, the Raman spectrum of surface-oxidized nanocrystals experience both a redshift, associated with quantum confinement, and a blueshift, promoted by compressive strain that increases continuously and monotonously as the oxide shell thickens. Ultimately, the interplay between these opposite effects leads to a net redshift that is lower than the one expected from confinement effects only, given by the $\Omega(\Gamma)_{\text{theo}}$ trend in Fig. 6.

The pressure exerted by the oxide shell in our Si NPs can be estimated considering the phonon pressure coefficient [51,52,104]. Assuming that the Si NPs are unstrained prior to the oxidation, i.e., the lattice is relaxed, and that they have the same compressibility of bulk *c*-Si, we can then estimate the hydrostatic pressure exerted by the growth of the oxide shell, i.e., quantify the strain, by means of the phonon pressure coefficient of bulk *c*-Si. The pressure coefficient describing the frequency shift of the optical phonon mode in bulk *c*-Si has been rigorously obtained by Ulrich *et al.* [105] at low temperature (6 K) and by other authors [106,107] at room temperature, with negligible differences. In this temperature range, the pressure coefficients are found to be nearly temperature independent, with variations within experimental errors [108,109]. Since, Ulrich and coauthors' work [105] is the only one reporting pressure coefficients for both the Raman frequency shift and linewidth, we will use their results in the following discussion. Accordingly, the linear pressure coefficient for the peak position is $d\Omega/dP = 5.10 \pm 0.04 \text{ cm}^{-1}/\text{GPa}$,

from which a compressive stress $\sigma = 1.2 \pm 0.4 \text{ GPa}$ is estimated for a frequency shift of approximately $6 \pm 2 \text{ cm}^{-1}$ (after long-term oxidation). Although the pressure-induced change in the Raman linewidth should be rather small [106,107,110], it can be estimated based on the linear pressure coefficient $d\Gamma/dP = 0.137 \pm 0.002 \text{ cm}^{-1}/\text{GPa}$ provided by Ulrich *et al.* [105]. Thus, the contribution of 1.2 GPa compressive stress to the Raman linewidth is merely of $0.16 \pm 0.05 \text{ cm}^{-1}$, well within our experimental error for determination of Γ from the Raman spectra. This shows that the presence of compressive strain in free-standing Si NPs owing to the growth of a superficial oxide contributes marginally to the Raman linewidth. This justifies the fact that the values of Γ of $\Omega(\Gamma)_{\text{exp}}$ and $\Omega(\Gamma)_{\text{theo}}$ in Fig. 6 are very similar. Finally, we would like to note that the stress values determined through the phonon pressure coefficient of bulk *c*-Si may be slightly underestimated. In fact, the phonon pressure coefficient in nanostructured silicon materials is often increased with respect to the bulk, as has been observed in SiO_2 -embedded silicon nanocrystals [111], silicon nanowires [112,113], and porous silicon [114–116].

In free-standing Si NPs, the nature of strain and how it evolves as the oxidation progresses is far from being understood. In fact, there is a general lack of consensus amongst the available literature, with both theoretical and experimental works reporting contradicting results about whether the strain is strictly compressive, tensile, or a mixture of both depending on the nanocrystal radius and on the extent of the surface oxidation. Yu and coworkers [46] investigated the structure of hydrogenated Si NPs using an empirical tight-binding approach and found a very small lattice contraction (0.01 to 0.02 \AA) in the atoms of the outermost two or three layers and an even smaller lattice expansion in the core of the nanocrystals. Conversely, by means of molecular dynamics simulations, Torre *et al.* [47] proposed that prior to the oxidation the nanocrystals (bare, not H-terminated) are under compression because of the surface curvature. In addition, they proposed that this compressive strain remains up to a few hundred oxygen atoms inserted in the nanocrystal surface, but then changes to tensile strain with the continuous incorporation of oxygen atoms up to an oxide thickness of the order of 15 \AA , and for thicker oxides the strain becomes compressive again. Our results seems to support the predictions of Yu *et al.* in the sense that the amount of strain prior to the oxidation is negligible. On the other hand, our work does not support the results of Torre *et al.*, since we find a continuously increasing compressive strain with increasing oxide thickness without any switching from compressive to tensile strain and vice versa.

Experimental works reporting strain in surface-oxidized free-standing Si NPs are scarce. Dhara and coworkers [40, 41,43] reported compressive strain in Si NPs of sizes in the range 5–43 nm and although they could not rule out

the presence of an ultra-thin amorphous oxide surface, they ascribed the strain as being mainly due to the formation of dislocations during the nanocrystal preparation by mechanical ball milling. In another work, comparing the luminescence of surface-oxidized free-standing nanocrystals versus matrix-embedded nanocrystals, Kusova *et al.* [42] proposed that the spontaneous growth of the oxide under ambient conditions does not exert any strain on the nanocrystal. In an electron microscopy study, Hofmeister *et al.* [45] concluded that surface-oxidized Si NPs with dimensions similar to the ones studied in the present work do not exhibit a sizeable strain. Unlike these reports, our work strongly suggests the presence of compressive strain in air-oxidized crystalline Si NPs.

The formation of compressive strain in our Si NPs along the oxidation is schematically illustrated in Fig. 7 and can be understood as follows. Prior to the oxidation, the nanocrystal surface is mostly passivated with Si—H bonds resulting from the silane decomposition during the plasma synthesis [3,4,35]. According to several investigations on similar Si NPs [91,117–119], the oxidation kinetics in H-terminated Si NPs can be explained based on the Cabrera-Mott theory [120]. Upon exposure of the nanocrystals to air, oxidizing species (O_2 and H_2O) are adsorbed at the surface and react with Si atoms, thereby initiating the oxide formation. Along this process, the superficial Si—H bonds are cleaved and replaced by silanol groups, which further promotes the adsorption of the oxidizing species due to its hydrophilic character [97,121]. As the oxidation progresses, the adsorbed oxidizing species, namely O_2 , diffuse through the freshly formed oxide towards the Si/SiO₂ interface, reacting with the Si atoms to form a new oxide layer (i.e., Si—O—Si bonds). According to the Cabrera-Mott theory, the oxide continues to thicken until the electric field that mediates the diffusion of O_2 decreases to a point where the growth rate is negligible, thus self-limiting the natural oxidation of the nanocrystal. Since the oxide shell is basically a disordered

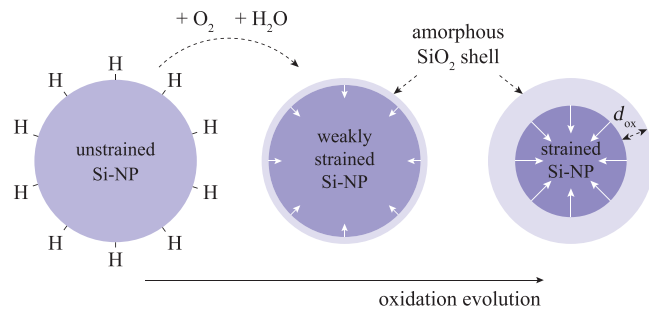


FIG. 7. Scheme of the evolution of oxidation and the resulting thickening of the oxide shell (d_{ox}) in a small Si NP, synthesized with a H-terminated surface. White arrows represent the continuous increase of compressive strain promoted by the thickening of the oxide shell.

(amorphous) structure and the Si—O—Si bonds are larger than the Si—Si bonds, the shell promotes a contraction of the nanocrystal core (likewise, a dilation of the oxide shell is expected). Thus, as soon as the oxidation starts, compressive strain appears in the nanocrystal core, and the Raman peak experiences a blueshift. The experimental observation of a continuously increasing blueshift, with respect to the theory [see $\Omega(\Gamma)_{theo}$ trend in Fig. 6], strongly points to the fact that the strain is compressive in nature throughout the whole oxidation process. We would like to note that, in principle, the compressive strain may influence the formation of the oxide itself, since incorporation of an O atom into strained Si—Si bonds could be energetically less favorable than into unstrained bonds. The quantitative analysis of such effects could be an interesting subject to be addressed in future studies by theoreticians working in this field.

Finally, it is of particular interest to note that the amount of stress exerted by the oxide shell in our free-standing Si NCs is noticeable lower than the stress values of the order of few GPa often determined experimentally [42,48–52,54,122] and predicted theoretically [53] for matrix-embedded Si NCs. This observation is related to the fact that the ultra-thin oxide shell in free-standing Si NCs can expand with less energetic effort (thermodynamically) than the expansion of an insulating matrix, which is the major volumetric element in matrix-embedded Si NCs behaving as a rigid interface. Thus, the lattice mismatches and thermal expansion mismatches play a much more decisive role when the Si NCs are embedded in a matrix environment than when the Si NCs are free standing.

IV. CONCLUSIONS

In conclusion, our study monitors the temporal evolution of physical phenomena related to the natural oxidation of Si NPs and sheds light on the nature of strain induced by a growing native oxide shell. For Si NPs with a surface termination with Si—H bonds (as-grown) and with an average size of approximately 3 nm, we find that the crystalline core of the Si NPs is virtually unstrained and the variations of the position and linewidth of the characteristic optical phonon Raman peak with respect to bulk *c*-Si are affected mostly by quantum-confinement effects. The exposure of the Si NPs to air leads to the growth of a native surface oxide and to a corresponding decrease of the nanocrystal size. The comparison of the measured Raman spectra with spectra simulated in the scope of an improved phonon-confinement model shows that the experimentally observed redshift of the nanocrystals Raman peak with respect to bulk *c*-Si is lower than that theoretically predicted considering solely confinement effects. This difference is ascribed to the appearance of compressive strain in the crystalline core of the Si NPs, which contributes as a blueshift of the Raman peak. The

compressive strain is found to increase continuously with the growth of the oxide shell throughout the whole oxidation process. The experimental and theoretical approaches applied in this study enabled a clear separation of the effects of phonon confinement and strain using the Raman spectrum of nanostructured materials.

Our results have major implications for the applicability of the Raman technique in the investigation of nanosilicon materials, in particular in the determination of nanocrystallite sizes. Due to the strongly surface-dependent lattice strain found for silicon nanocrystals, i.e., strain-free H-terminated nanocrystals and compressively strained oxide-terminated nanocrystals, and the large effect of strain on Raman spectra, the correlations between the investigated material properties and the characteristics of Raman spectra have to take into account the form of nanocrystal surface. Thus, correlations established for a specific surface termination may not be appropriate in the study of nanocrystals with a different form of surface termination.

ACKNOWLEDGMENTS

This work has been developed with the financial support from the Fundação para a Ciência e a Tecnologia (FCT) and FEDER through Projects No. UID/CTM/50025/2013, No. POCI-01-0145-FEDER-007688, and No. PTDC/CTM-ENE/2514/2012.

- [1] L. Pavesi, L. D. Negro, C. Mazzoleni, G. Franzó, and F. Priolo, Optical gain in silicon nanocrystals, *Nature* **408**, 440 (2000).
- [2] R. J. Anthony, D. J. Rowe, M. Stein, J. Yang, and U. Kortshagen, Routes to achieving high quantum yield luminescence from gas-phase-produced silicon nanocrystals, *Adv. Funct. Mater.* **21**, 4042 (2011).
- [3] L. Mangolini, Synthesis, properties, and applications of silicon nanocrystals, *J. Vac. Sci. Technol. B* **31**, 020801 (2013).
- [4] U. R. Kortshagen, R. M. Sankaran, R. N. Pereira, S. L. Girshick, J. J. Wu, and E. S. Aydil, Nonthermal plasma synthesis of nanocrystals: Fundamental principles, *Mater. Appl. Chem. Rev.* **116**, 11061 (2016).
- [5] K.-Y. Cheng, R. Anthony, U. R. Kortshagen, and R. J. Holmes, High-efficiency silicon nanocrystal light-emitting devices, *Nano Lett.* **11**, 1952 (2011).
- [6] B. Ghosh, Y. Masuda, Y. Wakayama, Y. Imanaka, J. Inoue, K. Hashi, K. Deguchi, H. Yamada, Y. Sakka, S. Ohki, T. Shimizu, and N. Shirahata, Hybrid white light emitting diode based on silicon nanocrystals, *Adv. Funct. Mater.* **24**, 7151 (2014).
- [7] D.-C. Wang, C. Zhang, P. Zeng, W.-J. Zhou, L. Ma, H.-T. Wang, Z.-Q. Zhou, F. Hu, S.-Y. Zhang, M. Lu, and X. Wu, An all-silicon laser based on silicon nanocrystals with high optical gains, *Sci. Bull.* **63**, 75 (2018).
- [8] A. M. P. Botas, C. D. S. Brites, J. Wu, U. Kortshagen, R. N. Pereira, L. D. Carlos, and R. A. S. Ferreira, A new generation of primary luminescent thermometers operating in different media based on silicon nanoparticles, *Part. Part. Syst. Charact.* **33**, 740 (2016).
- [9] C. M. Gonzalez and J. G. C. Veinot, Silicon nanocrystals for the development of sensing platforms, *J. Mater. Chem. C* **4**, 4836 (2016).
- [10] J. Wang, J. Guo, and J. Chen, Silicon nanocrystals with pH-sensitive tunable light emission from violet to blue-green, *Sensors* **17**, 2396 (2017).
- [11] A. Martínez, J. Blasco, P. Sanchis, J. V. Galán, J. García-Rupérez, E. Jordana, P. Gautier, Y. Lebour, S. Hernández, R. Spano, R. Guider, N. Daldosso, B. Garrido, J. M. Fedeli, L. Pavesi, and J. Martí, Ultrafast all-optical switching in a silicon-nanocrystal-based silicon slot waveguide at telecom wavelengths, *Nano Lett.* **10**, 1506 (2010).
- [12] R. Gresback, N. J. Kramer, Y. Ding, T. Chen, U. R. Kortshagen, and T. Nozaki, Controlled doping of silicon nanocrystals investigated by solution-processed field effect transistors, *ACS Nano* **8**, 5650 (2014).
- [13] P. Harvey-Collard, D. Drouin, and M. Pioro-Ladrière, A silicon nanocrystal tunnel field effect transistor, *Appl. Phys. Lett.* **104**, 193505 (2014).
- [14] R. N. Pereira, J. Coutinho, S. Niesar, T. A. Oliveira, W. Aigner, H. Wiggers, M. J. Rayson, P. R. Briddon, M. S. Brandt, and M. Stutzmann, Resonant electronic coupling enabled by small molecules in nanocrystal solids, *Nano Lett.* **14**, 3817 (2014).
- [15] W. Aigner, M. Wiesinger, H. Wiggers, M. Stutzmann, and R. N. Pereira, Three-dimensional percolation and performance of nanocrystal field-effect transistors, *Phys. Rev. Appl.* **5**, 054017 (2016).
- [16] G. Conibeer, M. Green, R. Corkish, Y. Cho, E.-C. Cho, C.-W. Jiang, T. Fangsuwannarak, E. Pink, Y. Huang, T. Puzzer, T. Trupke, B. Richards, A. Shalav, and K. lung Lin, Silicon nanostructures for third generation photovoltaic solar cells, *Thin Solid Films* **511**, 654 (2006).
- [17] C.-Y. Liu, Z. C. Holman, and U. R. Kortshagen, Optimization of Si NC/P3HT hybrid solar cells, *Adv. Funct. Mater.* **20**, 2157 (2010).
- [18] Y. Ding, R. Gresback, Q. Liu, S. Zhou, X. Pi, and T. Nozaki, Silicon nanocrystal conjugated polymer hybrid solar cells with improved performance, *Nano Energy* **9**, 25 (2014).
- [19] M. Dutta, L. Thirugnanam, P. V. Trinh, and N. Fukata, High efficiency hybrid solar cells using nanocrystalline Si quantum dots and Si nanowires, *ACS Nano* **9**, 6891 (2015).
- [20] D. Desta, S. K. Ram, R. Rizzoli, M. Bellettato, C. Summonte, B. R. Jeppesen, P. B. Jensen, Y.-C. Tsao, H. Wiggers, R. N. Pereira, P. Balling, and A. N. Larsen, Novel back-reflector architecture with nanoparticle based buried light-scattering microstructures for improved solar cell performance, *Nanoscale* **8**, 12035 (2016).
- [21] D. Neiner and S. M. Kauzlarich, Hydrogen-capped silicon nanoparticles as a potential hydrogen storage material: Synthesis, characterization, and hydrogen release, *Chem. Mater.* **22**, 487 (2010).
- [22] X. Su, Q. Wu, J. Li, X. Xiao, A. Lott, W. Lu, B. W. Sheldon, and J. Wu, Silicon-based nanomaterials for lithium-ion batteries: A review, *Adv. Energy Mater.* **4**, 1300882 (2014).

- [23] N. O'Farrel, A. Houlton, and B. R. Horrocks, Silicon nanoparticles: Applications in cell biology and medicine, *Int. J. Nanomed.* **1**, 451 (2006).
- [24] F. Erogbogbo, K.-T. Yong, I. Roy, R. Hu, W.-C. Law, W. Zhao, H. Ding, F. Wu, R. Kumar, M. T. Swihart, and P. N. Prasad, *In vivo* targeted cancer imaging, sentinel lymph node mapping and multi-channel imaging with biocompatible silicon nanocrystals, *ACS Nano* **5**, 413 (2011).
- [25] F. Peng, Y. Su, Y. Zhong, C. Fan, S.-T. Lee, and Y. He, Silicon nanomaterials platform for bioimaging, biosensing, and cancer therapy, *Acc. Chem. Res.* **47**, 612 (2014).
- [26] A. J. Almeida, H. Sugimoto, M. Fujii, M. S. Brandt, M. Stutzmann, and R. N. Pereira, Doping efficiency and confinement of donors in embedded and free standing Si nanocrystals, *Phys. Rev. B* **93**, 115425 (2016).
- [27] Z. Yang, M. Dasog, A. R. Dobbie, R. Lockwood, Y. Zhi, A. Meldrum, and J. G. C. Veinot, Highly luminescent covalently linked silicon nanocrystal/polystyrene hybrid functional materials: Synthesis, properties, and processability, *Adv. Funct. Mater.* **24**, 1345 (2014).
- [28] M. Dasog, G. B. D. los Reys, L. V. Titova, F. A. Hegmann, and J. G. C. Veinot, Size vs surface: Tuning the photoluminescence of freestanding silicon nanocrystals across the visible spectrum *via* surface groups, *ACS Nano* **8**, 9636 (2014).
- [29] K. Dohnalová, T. Gregorkiewicz, and K. Kusová, Silicon quantum dots: Surface matters, *J. Phys.: Condens. Matter* **26**, 173201 (2014).
- [30] B. Ghosh, M. Takeguchi, J. Nakamura, Y. Nemoto, T. Hamaoka, S. Chandra, and N. Shirahata, Origin of the photoluminescence quantum yields enhanced by alkane-termination of freestanding silicon nanocrystals: Temperature-dependence of optical properties, *Sci. Rep.* **6**, 36951 (2016).
- [31] B. Bruhn, B. J. M. Brenny, S. Dekker, I. Doğan, P. Schall, and K. Dohnalová, Multi-chromatic silicon nanocrystals, *Light Sci. Appl.* **6**, e17007 (2017).
- [32] M. Bürkle, M. Lozac'h, C. McDonald, D. Mariotti, K. Matsubara, and V. Švrček, Bandgap engineering in oh-functionalized silicon nanocrystals: Interplay between surface functionalization and quantum confinement, *Adv. Funct. Mater.* **27**, 1701898 (2017).
- [33] K. Dohnalová, I. Pelant, K. Kúsová, P. Gilliot, M. Gallart, O. Crégut, J.-L. Rehspringer, B. Hönerlage, T. Ostatnický, and S. Bakardjeva, Closely packed luminescent silicon nanocrystals in a distributed-feedback laser cavity, *New J. Phys.* **10**, 063014 (2008).
- [34] M. D. Bhatt and J. S. Lee, Effect of lattice strain on nanomaterials in energy applications: A perspective on experiment and theory, *Int. J. Hydrog. Energy* **42**, 16064 (2017).
- [35] J. Holm and J. T. Roberts, Modifying the composition of hydrogen-terminated silicon nanoparticles synthesized in a nonthermal rf plasma, *J. Vac. Sci. Technol. A* **28**, 161 (2010).
- [36] J. J. Wu, V. S. S. K. Kondeti, P. J. Bruggeman, and U. R. Kortshagen, Luminescent, water-soluble silicon quantum dots via micro-plasma surface treatment, *J. Phys. D: Appl. Phys.* **49**, 08LT02 (2016).
- [37] I. N. Germanenko, M. Dongol, Y. B. Pithawalla, M. S. El-Shall, and J. A. Carlisle, Effect of atmospheric oxidation on the electronic and photoluminescence properties of silicon nanocrystals, *Pure Appl. Chem.* **72**, 245 (2000).
- [38] A. Gupta and H. Wiggers, Freestanding silicon quantum dots: Origin of red and blue luminescence, *Nanotechnology* **22**, 055707 (2011).
- [39] A. M. P. Botas, R. A. S. Ferreira, R. N. Pereira, R. J. Anthony, T. Moura, D. J. Rowe, and U. Kortshagen, High quantum yield dual emission from gas-phase grown crystalline Si nanoparticles, *J. Phys. Chem. C* **118**, 10375 (2014).
- [40] S. Dhara and P. K. Giri, Size-dependent visible absorption and fast photoluminescence decay dynamics from freestanding strained silicon nanocrystals, *Nanoscale Res. Lett.* **6**, 320 (2011).
- [41] S. Dhara and P. K. Giri, Size dependent anisotropic strain and optical properties of strained Si nanocrystals, *J. Nanosci. Nanotechnol.* **11**, 9215 (2011).
- [42] K. Kúsová, L. Ondič, E. Klimesová, K. Herynková, I. Pelant, S. Daniš, J. Valenta, M. Gallart, M. Ziegler, B. Hönerlage, and P. Gilliot, Luminescence of freestanding versus matrix-embedded oxide-passivated silicon nanocrystals: The role of matrix-induced strain, *Appl. Phys. Lett.* **101**, 143101 (2012).
- [43] S. Dhara, K. Imakita, P. K. Giri, and M. Fujii, Strain dependence of the nonlinear optical properties of strained Si nanoparticles, *Opt. Lett.* **39**, 3833 (2014).
- [44] K. Kúsová, P. Hapala, J. Valenta, P. Jelínek, O. Cibulka, L. Ondič, and I. Pelant, Direct bandgap silicon: Tensile-strained silicon nanocrystals, *Adv. Mater. Interfaces* **1**, 1300042 (2014).
- [45] H. Hofmeister, F. Huisken, and B. Kohn, Lattice contraction in nanosized silicon particles produced by laser pyrolysis of silane, *Eur. Phys. J. D* **9**, 137 (1999).
- [46] D. K. Yu, R. Q. Zhang, and S. T. Lee, Structural properties of hydrogenated silicon nanocrystals and nanoclusters, *J. Appl. Phys.* **92**, 7453 (2002).
- [47] J. D. Torre, J.-L. Bocquet, Y. Limoge, J.-P. Crocombe, E. Adam, G. Martin, T. Baron, P. Rivallin, and P. Mur, Study of self-limiting oxidation of silicon nanoclusters by atomistic simulations, *Appl. Phys. Lett.* **92**, 1084 (2002).
- [48] T. Arguirov, T. Mchedlidze, M. Kittler, R. Rölver, B. Berghoff, M. Först, and B. Spangenberg, Residual stress in Si nanocrystals embedded in a SiO₂ matrix, *Appl. Phys. Lett.* **89**, 053111 (2006).
- [49] S. Yerci, U. Serincan, I. Dogan, S. Tokay, M. Genisel, A. Aydinli, and R. Turan, Formation of silicon nanocrystals in sapphire by ion implantation and the origin of visible photoluminescence, *J. Appl. Phys.* **100**, 074301 (2006).
- [50] L. Khriachtchev, M. Räsänen, and S. Novikov, Laser-controlled stress of Si nanocrystals in a free-standing Si/SiO₂ superlattice, *Appl. Phys. Lett.* **88**, 013102 (2006).
- [51] S. Hernández, A. Martínez, P. Pellegrino, Y. Lebour, B. Garrido, E. Jordana, and J. M. Fedeli, Silicon nanocluster crystallization in SiO_x films studied by Raman scattering, *J. Appl. Phys.* **104**, 044304 (2008).
- [52] G. Zatyb, A. Podhorodecki, X. J. Hao, J. Misiewicz, Y. S. Shen, and M. A. Green, Correlation between stress and

- carrier nonradiative recombination for silicon nanocrystals in an oxide matrix, *Nanotechnology* **22**, 335703 (2011).
- [53] K. Kleovoulou and P. C. Kelires, Stress state of embedded Si nanocrystals, *Phys. Rev. B* **88**, 085424 (2013).
- [54] J. Jettanasen, Study of silicon nanoparticles in dielectric oxides obtained by solgel route, *J. Exp. Nanosci.* **10**, 1319 (2015).
- [55] A. Wellner, V. Paillard, C. Bonafos, H. Coffin, A. Claverie, B. Schmidt, and K. H. Heinig, Stress measurements of germanium nanocrystals embedded in silicon oxide, *J. Appl. Phys.* **94**, 5639 (2003).
- [56] Y. M. Yang, X. L. Wu, L. W. Yang, G. S. Huang, G. G. Siu, and P. K. Chu, Low-frequency Raman scattering of Ge and Si nanocrystals in silica matrix, *J. Appl. Phys.* **98**, 064303 (2005).
- [57] E. S. F. Neto, N. O. Dantas, S. W. da Silva, P. C. Morais, and M. A. P. da Silva, Confirming the lattice contraction in CdSe nanocrystals grown in a glass matrix by Raman scattering, *J. Raman Spectrosc.* **41**, 1302 (2010).
- [58] G. Scamarcio, M. Lugará, and D. Manno, Size-dependent lattice contraction in CdS_{1-x}Se_x nanocrystals embedded in glass observed by Raman scattering, *Phys. Rev. B* **45**, 13792 (1992).
- [59] N. Tschirner, H. Lange, A. Schliwa, A. Biermann, C. Thomsen, K. Lambert, R. Gomes, and Z. Hens, Interfacial alloying in CdSe/CdS heteronanostructures: A Raman spectroscopy analysis, *Chem. Mater.* **24**, 311 (2012).
- [60] J. Knipping, H. Wiggers, B. Rellinghaus, P. Roth, D. Konjehodzic, and C. Meier, Synthesis of high purity silicon nanoparticles in a low pressure microwave reactor, *J. Nanosci. Nanotechnol.* **4**, 1039 (2004).
- [61] L. Mangolini, E. Thimsen, and U. Kortshagen, High-yield plasma synthesis of luminescent silicon nanocrystals, *Nano Lett.* **5**, 655 (2005).
- [62] U. Kortshagen, Nonthermal plasma synthesis of semiconductor nanocrystals, *J. Phys. D: Appl. Phys.* **42**, 113001 (2009).
- [63] Z. Ni, X. Pi, M. Ali, S. Zhou, T. Nozaki, and D. Yang, Freestanding doped silicon nanocrystals synthesized by plasma, *J. Phys. D: Appl. Phys.* **48**, 314006 (2015).
- [64] İ. Dogan, R. H. J. Westermann, K. Dohnalová, A. H. M. Smets, M. A. Verheijen, T. Gregorkiewicz, and M. C. M. van de Sanden, Ultrahigh throughput plasma processing of free standing silicon nanocrystals with lognormal size distribution, *J. Appl. Phys.* **113**, 134306 (2013).
- [65] İ. Dogan and M. C. M. van de Sanden, Direct characterization of nanocrystal size distribution using Raman spectroscopy, *J. Appl. Phys.* **114**, 134310 (2013).
- [66] L. Han, M. Zeman, and A. H. M. Smets, Size control, quantum confinement, and oxidation kinetics of silicon nanocrystals synthesized at a high rate by expanding thermal plasma, *Appl. Phys. Lett.* **106**, 213106 (2015).
- [67] I. F. Crowe, M. P. Halsall, O. Hulko, A. P. Knights, R. M. Gwilliam, M. Wojdak, and A. J. Kenyon, Probing the phonon confinement in ultrasmall silicon nanocrystals reveals a size-dependent surface energy, *J. Appl. Phys.* **109**, 083534 (2011).
- [68] B. P. Falcão, J. P. Leitão, H. Águas, and R. N. Pereira, Raman spectrum of nanocrystals: Phonon dispersion splitting and anisotropy, *Phys. Rev. B* **98**, 195406 (2018).
- [69] J. Langford and A. Wilson, Scherrer after sixty years: A survey and some new results in the determination of crystallite size, *J. Appl. Cryst.* **11**, 102 (1978).
- [70] G. Mauckner, K. Thonke, and R. Sauer, Dynamics of the degradation by photo-oxidation of porous silicon: FITL and FTIR absorption study, *J. Phys.: Condens. Matter* **5**, L9 (1993).
- [71] R. R. Koropecski, R. D. Arce, and J. A. Schmidt, Photo-oxidation effects in porous silicon luminescence, *Phys. Rev. B* **69**, 205317 (2004).
- [72] S. Aouida, M. Saadoun, K. B. Saad, and B. Bessais, UV photo-oxidation induced structural and photoluminescence behaviors in vapor-etching based porous silicon, *Mater. Sci. Eng. C* **26**, 495 (2006).
- [73] B. P. Falcão, J. P. Leitão, M. R. Correia, M. R. Soares, H. Wiggers, A. Cantarero, and R. N. Pereira, Light-induced nonthermal population of optical phonons in nanocrystals, *Phys. Rev. B* **95**, 115439 (2017).
- [74] I. Iatsunskiy, G. Nowaczyk, S. Jurga, V. Fedorenko, M. Pavlenko, and V. Smyntyna, One and two-phonon Raman scattering from nanostructured silicon, *Optik* **126**, 1650 (2015).
- [75] A. Valentin, J. Sée, S. Galdin-Retailleau, and P. Dollfus, Study of phonon modes in silicon nanocrystals using the adiabatic bond charge model, *J. Phys. Condens. Matter* **20**, 145213 (2008).
- [76] K. H. Khoo, A. T. Zayak, H. Kwak, and J. R. CheLIKowsky, First-Principles Study of Confinement Effects on the Raman Spectra of Si Nanocrystals, *Phys. Rev. Lett.* **105**, 115504 (2010).
- [77] Y. Gao, X. Zhao, P. Yin, and F. Gao, Size-dependent Raman shifts for nanocrystals, *Sci. Rep.* **6**, 20539 (2016).
- [78] Y. Gao and P. Yin, Origin of asymmetric broadening of Raman peak profiles in Si nanocrystals, *Sci. Rep.* **7**, 43602 (2017).
- [79] M. H. Brodsky, M. Cardona, and J. J. Cuomo, Infrared and Raman spectra of the silicon-hydrogen bonds in amorphous silicon prepared by glow discharge and sputtering, *Phys. Rev. B* **16**, 3556 (1977).
- [80] A. Zwick and R. Caries, Multiple-order Raman scattering in crystalline and amorphous silicon, *Phys. Rev. B* **48**, 6024 (1993).
- [81] J. Leburton, J. Pascual, and C. M. F. Torres, eds., *Phonons in Semiconductor Nanostructures*, Nato Science Series E: Applied Sciences (Springer Science+Business Media Dordrecht, Netherlands, 1993), Vol. 236.
- [82] S. Dhanekar, S. S. Islam, T. Islam, A. K. Shukla, and Harsh, Organic vapour sensing by porous silicon: Influence of molecular kinetics in selectivity studies, *Phys. E* **42**, 1648 (2010).
- [83] V. A. Volodin and D. I. Koshelev, Quantitative analysis of hydrogen in amorphous silicon using Raman scattering spectroscopy, *J. Raman Spectrosc.* **44**, 1760 (2013).
- [84] C. S. Wang, J. M. Chen, R. Becker, and A. Zdetsis, Second order Raman spectrum and phonon density of states of silicon, *Phys. Rev.* **44**, 517 (1973).
- [85] P. Mishra and K. P. Jain, First- and second-order Raman scattering in nanocrystalline silicon, *Phys. Rev. B* **64**, 073304 (2001).

- [86] J. J. H. Parker, D. W. Feldman, and M. Ashkin, Raman scattering by silicon and germanium, *Phys. Rev.* **155**, 712 (1967).
- [87] S. Khachadorian, H. Scheel, A. Colli, A. Vierck, and C. Thomsen, Temperature dependence of first- and second-order Raman scattering in silicon nanowires, *Phys. Stat. Sol. b* **247**, 3084 (2010).
- [88] V. G. Kravets and V. Y. Kolmykova, Raman scattering of light in silicon nanostructures: First- and second-order spectra, *Opt. Spectrosc.* **99**, 75 (2005).
- [89] L. V. Mercaldo, E. M. Esposito, P. D. Veneri, G. Fameli, S. Mirabella, and G. Nicotra, First and second-order Raman scattering in Si nanostructures within silicon nitride, *Appl. Phys. Lett.* **97**, 153112 (2010).
- [90] S. Scamarcio, V. Spagnolo, G. Ventruti, and M. Lugara, Size dependence of electron-LO-phonon coupling in semiconductor nanocrystals, *Phys. Rev. B* **53**, 10489 (1996).
- [91] R. N. Pereira, D. J. Rowe, R. J. Anthony, and U. Kortshagen, Oxidation of freestanding silicon nanocrystals probed with electron spin resonance of interfacial dangling bonds, *Phys. Rev. B* **83**, 155327 (2011).
- [92] R. N. Pereira, D. J. Rowe, R. J. Anthony, and U. Kortshagen, Freestanding silicon nanocrystals with extremely low defect content, *Phys. Rev. B* **86**, 085449 (2012).
- [93] D. C. Marra, E. A. Edelberg, R. L. Naone, and E. S. Aydil, Silicon hydride composition of plasma-deposited hydrogenated amorphous and nanocrystalline silicon films and surfaces, *J. Vac. Sci. Technol. A* **16**, 3199 (1998).
- [94] J. Holm and J. T. Roberts, Surface chemistry of aerosolized silicon nanoparticles: Evolution and desorption of hydrogen from 6-nm diameter particles, *J. Am. Chem. Soc.* **129**, 2496 (2007).
- [95] J. Holm and J. T. Roberts, Thermal oxidation of 6 nm aerosolized silicon nanoparticles: Size and surface chemistry changes, *Langmuir* **23**, 11217 (2007).
- [96] X. D. Pi, L. Mangolini, S. A. Campbell, and U. Kortshagen, Room-temperature atmospheric oxidation of silicon nanocrystals after HF etching, *Phys. Rev. B* **75**, 085423 (2007).
- [97] T. Miura, M. Niwano, D. Shoji, and N. Miyamoto, Kinetics of oxidation on hydrogen-terminated Si(100) and(111) surfaces stored in air, *J. Appl. Phys.* **79**, 4373 (1996).
- [98] B. B. Stefanov, A. B. Gurevich, M. K. Weldon, K. Raghavachari, and Y. J. Chabal, Silicon epoxide: Unexpected intermediate during silicon oxide formation, *Phys. Rev. Lett.* **81**, 3908 (1998).
- [99] C. Aharoni and F. C. Tompkins, Kinetics of adsorption and desorption and the Elovich equation, *Adv. Catal.* **21**, 1 (1970).
- [100] L. Han, M. Zeman, and A. H. M. Smets, Raman study of laser-induced heating effects in free-standing silicon nanocrystals, *Nanoscale* **7**, 8389 (2015).
- [101] G. Ledoux, O. Guillois, D. Porterat, C. Reynaud, F. Huisken, B. Kohn, and V. Paillard, Photoluminescence properties of silicon nanocrystals as a function of their size, *Phys. Rev. B* **62**, 15942 (2000).
- [102] T. Nozaki, K. Sasaki, T. Ogino, D. Asahi, and K. Okazaki, Microplasma synthesis of tunable photoluminescent silicon nanocrystals, *Nanotechnology* **18**, 235603 (2007).
- [103] See Supplemental Material at <http://link.aps.org/supplemental/10.1103/PhysRevApplied.11.024054> for details of the evolution of size distribution as a function of oxidation.
- [104] J. S. Reparaz, A. Bernardi, A. R. G. Ni, P. D. Lachar-moise, M. I. Alonso, M. Garriga, J. Novák, and I. Vávra, Phonon pressure coefficient as a probe of the strain status of self-assembled quantum dots, *Appl. Phys. Lett.* **91**, 081914 (2007).
- [105] C. Ulrich, E. Anastassakis, K. Syassen, A. Debernardi, and M. Cardona, Lifetime of phonons in semiconductors under pressure, *Phys. Rev. Lett.* **78**, 1283 (1997).
- [106] B. A. Weinstein and G. J. Piermarini, Raman scattering and phonon dispersion in Si and GaP at very high pressure, *Phys. Rev. B* **12**, 1172 (1975).
- [107] T. P. Mernagh and L.-G. Liu, Pressure dependence of raman phonons of some group IVA (C, Si, and Ge) elements, *J. Phys. Chem. Solids* **52**, 507 (1991).
- [108] E. Liarokapis, E. Anastassakis, and G. A. Kourouklis, Raman study of phonon anharmonicity in LaF₃, *Phys. Rev. B* **32**, 8346 (1985).
- [109] E. Sarantopoulou, C. Raptis, S. Ves, D. Christofilos, and G. A. Kourouklis, Temperature and pressure dependence of raman-active phonons of CaMoO₄: An anharmonicity study, *J. Phys. Condens. Matter* **14**, 8925 (2002).
- [110] A. Bernardi, C. Ulrich, M. Cardona, and K. Syassen, Pressure dependence of raman linewidth in semiconductors, *Phys. Stat. Sol. (b)* **223**, 213 (2001).
- [111] J. Ibáñez, S. Hernández, J. López-Vidrier, D. Hiller, S. Gutsch, M. Zacharias, A. Segura, J. Valenta, and B. Garrido, Optical emission from SiO₂-embedded silicon nanocrystals: A high-pressure Raman and photoluminescence study, *Phys. Rev. B* **92**, 035432 (2015).
- [112] S. Khachadorian, K. Papagelis, H. Scheel, A. Colli, A. C. Ferrari, and C. Thomsen, High pressure Raman scattering of silicon nanowires, *Nanotechnology* **22**, 195707 (2011).
- [113] Y. Wang, J. Zhang, J. Wu, J. L. Coffer, Z. Lin, S. V. Sinogeikin, W. Yang, and Y. Zhao, Phase transition and compressibility in silicon nanowires, *Nano Lett.* **8**, 2891 (2008).
- [114] K. Barla, R. Herino, G. Bomchil, J. C. Pfister, and A. Freund, Determination of lattice parameter and elastic properties of porous silicon by x-ray diffraction, *J. Cryst. Growth* **68**, 727 (1984).
- [115] D. Bellet and G. Dolino, X-ray diffraction studies of porous silicon, *Thin Solid Films* **276**, 1 (1996).
- [116] D. Papadimitriou, Y. S. Raptis, A. G. Nassiopoulou, and G. Kaltsas, Porous silicon of variable porosity under high hydrostatic pressure: Raman and photoluminescence studies, *Phys. Stat. Sol. (a)* **165**, 43 (1998).
- [117] X. D. Pi, R. Gresback, R. W. Liptak, S. A. Campbell, and U. Kortshagen, Doping efficiency, dopant location, and oxidation of silicon nanocrystals, *Appl. Phys. Lett.* **92**, 123102 (2008).
- [118] R. W. Liptak, U. Kortshagen, and S. A. Campbell, Surface chemistry dependence of native oxidation formation on silicon nanocrystals, *J. Appl. Phys.* **106**, 064313 (2009).
- [119] R. Gresback, T. Nozaki, and K. Okazaki, Synthesis and oxidation of luminescent silicon nanocrystals from silicon

- tetrachloride by very high frequency nonthermal plasma, [Nanotechnology](#) **22**, 305605 (2011).
- [120] N. Cabrera and N. F. Mott, Theory of the oxidation of metals, [Rep. Prog. Phys.](#) **12**, 163 (1949).
- [121] M. Niwano, J. Kageyama, K. Kurita, K. Kinashi, I. Takahashi, and N. Miyamoto, Infrared spectroscopy study of initial stages of oxidation of hydrogen-terminated Si surfaces stored in air, [J. Appl. Phys.](#) **76**, 2157 (1994).
- [122] C.-H. Cho, J.-W. Kang, I.-K. Park, and S.-J. Park, Enhanced quantum confinement in tensile-strained silicon nanocrystals embedded in silicon nitride, [Curr. Appl. Phys.](#) **17**, 1616 (2017).